Revealing strain effects on the chemical composition of perovskite oxide thin films surface, bulk and interfaces

Celeste A. M. van den Bosch, Andrea Cavallaro, Roberto Moreno, Giannantonio Cibin, Gwilherm Kerherve, José M. Caicedo, Thomas K. Lippert, Max Doebeli, José Santiso, Stephen J. Skinner and Ainara Aguadero**

Dr. Celeste A. M. van den Bosch, Dr. Andrea Cavallaro, Dr. Gwilherm Kerherve, Prof. Stephen J. Skinner, Dr. Ainara Aguadero
Department of Materials, Imperial College, London SW7 2AZ, United Kingdom
E-mail: cav09@imperial.ac.uk; a.aguadero@imperial.ac.uk

Roberto Moreno, José M. Caicedo, Dr. José Santiso
ICN2, Institut Catalá de Nanociéncia i Nanotecnologia, Campus UAB, 08913 Bellaterra, Barcelona, Spain

Dr. Giannanonio Cibin
Diamond Light Source Ltd., Diamond House, Harwell Science and Innovation Campus, Didcot, Oxfordshire OX11 0DE, United Kingdom

Prof. Dr. Thomas K. Lippert
Laboratory for Multiscale Materials Experiments (LMX), Paul Scherrer Institute, 5232 Villigen, Switzerland

Prof. Dr. Thomas K. Lippert
Department of Chemistry and Applied Biosciences, Laboratory of Inorganic Chemistry, ETH Zurich, Switzerland

Dr. Max Doebeli
Laboratory of Ion Beam Physics, ETH Zurich, 8093 Zurich, Switzerland

Dr. José Santiso
CSIC, Consejo Superior de Investigaciones Científicas, ICN2 Building, Campus UAB, 08193 Bellaterra, Barcelona, Spain

Keywords: in situ, epitaxial thin films, chemical expansion, strain engineering, interfaces

Abstract

Understanding the effects of lattice strain on oxygen surface and diffusion kinetics in oxides is a controversial subject that is critical for developing efficient energy storage and conversion materials. In this work, high-quality epitaxial thin films of the model perovskite $La_{0.5}Sr_{0.5}Mn_{0.5}Co_{0.5}O_{3-\delta}$ (LSMC), under compressive or tensile strain, were characterized with a combination of *in situ* and *ex situ* bulk and surface-sensitive techniques. The results demonstrate a non-linear correlation of mechanical and chemical properties as a function of the operation conditions. It was observed that the effect of strain on reducibility is dependent on the "effective strain" induced on the chemical bonds. In plain strain, and in particular the relative B-O length bond, are the key factor controlling which of the B-site cation would be reduced preferentially. Furthermore, the need to use a set of complimentary techniques to

isolate different chemically-induced strain effects was proven. With this, it was confirmed that tensile strain favors the stabilization of a more reduced lattice, accompanied by greater segregation of strontium secondary phases and a decrease of oxygen exchange kinetics on LSMC thin films.

1. Introduction

Developing new oxide materials with high ionic and electronic conductivity and fast oxygen surface exchange kinetics is crucial for optimizing performance in a range of device applications including solid oxide fuel cells (SOFCs), batteries and permeation membranes. The structure and chemistry of surfaces is largely responsible for key reactions that determine device performance. Surfaces can dramatically deviate from the bulk due to the interruption of symmetry which results in a different surface free energy. Understanding the composition and structure of surfaces is therefore critically important for designing surfaces and interfaces with high reactivity and stability.

Nanoscale oxide thin films have been used in investigations of oxide properties for SOFCs,[1,2] batteries,[3–5] catalysts,[6] sensors[7] and redox-based memristors[8–10]. Strain can be introduced into these systems via lattice mismatch at interfaces and has been reported to affect properties including ionic and electronic conductivity,[11,12] activation energy,[13,14] critical temperatures for superconductors,[15] and cation segregation[16]. In strained thin films it is generally accepted that greater tensile strain weakens interatomic bonds and therefore lowers vacancy formation enthalpy and the energy barriers of both vacancy migration and dissociation.[17] However work on strained systems has resulted in, sometimes, controversial and contradictory reports of strain modifying surface reaction kinetics and degradation effects.[18,19]

Perovskite oxides are a flexible family of materials with the general structure $A_{1-x}A'_xB_{1-y}B'_yO_{3-\delta}$. Previous work has attempted to predict perovskite behavior based on various indicators such as correlating electronic structure and reaction kinetics and relating conductivity changes to strain in thin films[17]. The link between electronic structure and reactivity is derived from the well-established relationship between reactivity and the *d*-band centre relative to the Fermi level in strained metals.[20,21] For perovskites, the e_g occupancy has been investigated as a descriptor for oxygen reduction reaction catalysis[22,23] and some reports demonstrated experimentally that catalytic activity of perovskite oxides is dependent on the concentration of oxygen vacancies, and the B-site cation valence state.[24–26]

$La_{1-x}Sr_xCoO_3$ (LSC) and $La_{1-x}Sr_xMnO_3$ (LSM) are two of the most widely studied cathode materials for SOFCs. The investigation of thin film LSC by Klenov et al.[27] (x = 0.5) at temperatures up to 600°C suggested the oxygen vacancy structure of LSC on $SrTiO_3$ (STO) and $LaAlO_3$ (LAO) substrates is related to the presence of both thermal and physical strain. More recently, oxygen surface exchange and diffusion kinetics studies by Kubicek et al.[28] (x = 0.2 and 0.4), in the temperature range 280 to 475°C , as well as surface and electronic structure studies of Cai et al.[29] (x = 0.2), from room temperature to 450°C, demonstrated that the activity of LSC can be enhanced with tensile strain. Cai et al. propose three mechanisms for the electronic structure differences they report in strained LSC thin films, namely: cobalt spin-state transitions, electronic bandwidth broadening due to structural changes and formation of oxygen vacancies modifying the d-band structure of the cobalt, concluding that the oxygen defect structure is responsible.

Studies of strontium-containing perovskites frequently highlight substantial strontium segregation, a primary cathode degradation mechanisms in SOFCs due to a reduction of active surface sites and related phase changes, at thin film surfaces.[30] Dulli et al.[31] linked strontium

segregation in the perovskite LSM (x = 0.35) to a surface layer restructuring to a Ruddlesden-Popper (RP) phase, after their films were annealed at 900°C. The reverse has also been reported by Chen et al.[32] with a $(La_{1-x}Sr_x)_2CoO_4$ (x = 0.25, 0.5) RP-phase surface restructuring of the first three unit cells, due to strontium segregation, to the perovskite LSC after annealing in an oxygen-enriched atmosphere. For perovskite LSM (x = 0.3), Jalili et al.[33] report enhancement of both strontium segregation and oxygen vacancy formation, at room temperature and 500°C, in thin films under tensile strain. The enhancement is primarily attributed to structurally induced bond length changes, i.e. chemical expansion. Further works also concluded that lattice expansion, related to tensile strain, is a key factor for promoting surface cation segregation.[34,35]

This work investigates thin films of $La_{0.5}Sr_{0.5}Mn_{0.5}Co_{0.5}O_{3-\delta}$ (LSMC), which has the highest reported oxygen stoichiometry range in a perovskite system.[36] LSMC can accommodate two distinct structures, a hexagonal *R3c̄* stoichiometric (δ = 0) and an orthorhombic *Pbnm* hypo-stoichiometric (up to δ= 0.62). The catalytic activity and selectivity of the oxidized and reduced LSMC phases for the oxidation of hydrocarbons was suggested to be related to the oxygen content and transition metal oxidation states, indicating that control of oxygen stoichiometry allows the catalytic behavior of these phases to be tuned.[36] This difference in catalytic behavior, linked to the defect structure, makes LSMC an intriguing material for the study of oxygen stoichiometry control. Double substitution at both the A- and B- perovskite sites, provides scope for building on work of simpler perovskite systems with single occupancy of the B-site, for understanding key mechanisms at the surface of perovskite thin films.

2. Results & Discussion

2.1. Structural Characterization

To explore the effects of strain on the properties of LSMC, epitaxial thin films were deposited under oxidizing conditions by pulsed laser deposition (PLD) on (001) single crystal substrates: $LaAlO_3$ (LAO), $(LaAlO_3)_{0.3}(Sr_2AlTa_6)_{0.7}$ (LSAT) and $SrTiO_3$ (STO). The mismatch of the pseudocubic oxidized LSMC, relative to the single crystal substrates, resulted in tensile strain of 1.40 % for STO and 0.44 % for LSAT and compressive strain of -1.68 % for LAO. For films on the three substrates, denoted as LSMC/LAO, LSMC/STO and LSMC/LSAT, a combination of X-ray diffraction (XRD), reflectivity (XRR) and reciprocal space mapping (RSM) measurements was used to confirm high-quality, strained epitaxial growth, measure thin film thickness and calculate the unit cell volume for the as-deposited thin films (see Figures S1-S3). As expected for strained films, in-plane compression is accompanied by out-of-plane elongation, and vice versa, an elastic response often called the Poisson effect.[37] **Figure 1** shows the inverse relationship between the in-plane and out-of-plane cell parameters of LSMC with strain and the total volume of the strained unit cells. The structural data confirms that lattice strain of LSMC thin films is directly linked to the average unit cell volume, with tensile strain resulting in the highest volume and compressive strain resulting in the lowest unit cell volume.

Previous work on other perovskite thin film systems has demonstrated that strain can be used to alter reaction kinetics.[38–40] XRD allows for very accurate determination of cell parameters (below 10×10^{-3} Å) and has been demonstrated as a measurement technique for *in situ* monitoring of thin film cell structure variations related to oxidation and reduction, facilitating direct correlation of structural changes with redox activity upon exposure to step changes between different atmospheres.[41–43] The detection limit of this *in situ* XRD technique is significantly smaller than expansion of the pseudocubic bulk LSMC cell parameters from 3.8511 to 3.8871 Å, for the oxidized and reduced phases respectively, when heated under 5 % H_2 / balance N_2, a lattice parameter expansion of 3.6×10^{-2} Å or 0.94 %.

In epitaxial thin films, matching between in-plane cell parameters of the substrate and the thin film inhibits changes in the thin film layer, therefore the in-plane cell parameter of LSMC is not expected to vary significantly due to changes of the atmosphere.[41] During *in situ* XRD measurements (see Figure S4a), the films were heated (600 to 750°C), aligned to observe the $\bar{1}03$ asymmetric film reflection and cycled between a synthetic air (~ 2.1 x 10^5 ppm O_2, 20 % O_2 / 80 % N_2) and nitrogen (~ 10 ppm O_2, 100 % N_2) atmosphere. Within the scan range of $\Delta 2\theta$ = 2.5°, a $\bar{1}03$ substrate reflection tail was also observed, which was used as an internal reference (see Figure S5). Each 2.5° 2θ scan was fitted using a two-peak, pseudo-Voigt fit (see Figure S6) and the LSMC peak position was used to calculate the out-of-plane cell parameter relative to the substrate to account for any film peak shift due to sample misalignment during the experiment.

For both compressive (LSMC/LAO) and tensile (LSMC/STO) strain, oxidation of the films on switching from low to high pO_2 is a consistently faster process than the reduction process, occurring when switching from high to low pO_2. For example, for LSMC/LAO at 750 °C (see **Figure 2**), the film takes 75 to 80 min to reduce by approximately 95 % of the measured maximum reduction, within a given cycle. On oxidation at the same temperature, the film takes 70 to 100 s to reach approximately 100 % of the original cell parameter. Further, using a double exponential, with time constants $t_1 < t_2$, provides a better fit in the fitting of the reduction process however the oxidation is best described by a single component, with time constant t_1 only. Part of the asymmetry between oxidation and reduction may be accounted for by the large pO_2 step change used in the *in situ* XRD experimental setup, necessary to obtain a measurable change in the cell parameter, as similar materials have different exchange values depending on the pO_2. The difference in time for oxidation and reduction, as well as the number of fitting parameters, could also suggest that the oxygen reduction and evolution reactions follow different reaction pathways, possibly due to slower re-equilibration of the sample, including an equilibration of oxygen at the interface between the film and substrate, after a fast oxygen surface exchange. An additional equilibration step would depend on the energy barriers for oxygen transport and the energetics of oxygen vacancy formation across the interface of the film and substrate, as well as oxygen diffusion in the substrate. For application in SOFCs as a cathode, the material would be exposed to a high pO_2 and therefore would always have a larger exchange value. The difference in reaction rates has consequences for applications requiring the use of both oxygen evolution and reduction with large pO_2 changes, including metal-air batteries, as the rate of oxygen incorporation and evolution impacts charge and discharge rates.

The *in situ* XRD measurements were performed with reduction in a nitrogen atmosphere, resulting in the expansion of the out-of-plane cell parameter by up to 3.9 x 10^{-3} Å or 0.10 % for the film on LAO. Surface exchange coefficients were calculated by fitting cell parameter profiles, following the method described by Moreno and Santiso et al.[41–43] (see Figure S7). The change between the relative, average oxidized and reduced cell parameters for each temperature shows a greater change in the magnitude of the cell parameter for films under compressive strain (see Figure 2c). This could be related to the STO film being more reduced from the beginning as proven by XANES analysis (see section 2.2. Chemical Characterization), and therefore, experiencing a lower driving force for reduction under the nitrogen atmosphere used during the experiment. When looking to the reaction kinetics, it seems that K_{oxi} for the LAO films is bigger than for the STO film in the first cycle. This should be related to the lower energy required for oxidation in LSCM under compressive strain. The kinetics deterioration in the second cycle should be related to the passivation of the surface due to further Sr segregation as suggested by previous studies. It should be noted that the passivation effect could be bigger under reduction due to an enhancement of the Schottky defects in the perovskites for which the generation of oxygen vacancies can be accompanied by the creation of Sr vacancies in

competition with the reduction of the lattice. This could be an additional factor to explain the slower reduction kinetics compared to the oxidation observed. The Arrhenius plots suggest a transition at 650 °C (Figure 2d-e), however the process responsible for this transition has not yet been identified. It has previously been noted that exchange coefficients for slow diffusers are relatively scattered, as in tracer diffusion experiments by De Souza and Kilner[44,45], and contribute to large inaccuracies in $k_{exchange}$ values. The error bars in Figure 2d-e are based on fitting the data with an exponential factor and therefore do not fully account for experimental errors such as temperature stability.

2.2. Chemical Characterization

Unit cell volume and defect chemistry are closely connected through chemical expansion and changes in lattice parameter due to strain are expected to promote a change in defect concentration.[46] Cai et al.[29] suggest chemical expansion as the primary reason for the impact of strain on the electronic properties of strained LSC and Jalili et al.[33] suggest chemical expansion as a key driving force for differences in strontium segregation in LSM. Following the theory of chemical expansion, based on the structural data and in the absence of a dominant accommodation of the structural changes by compositional changes at the A- and B-sites, LSMC/LAO is expected to accommodate the highest transition metal oxidation states as it has the smallest unit cell volume (56.57 ± 0.29 $Å^3$). LSMC/STO has the largest unit cell volume (58.59 ± 0.13 $Å^3$), suggesting the lowest transition metal oxidation states. This assumption was investigated using a wide range of techniques to probe the chemical composition of the thin films. Oxidation states were analyzed using X-ray absorption near edge spectroscopy (XANES). The elemental composition of the LSMC thin films was determined using ion scattering techniques: Rutherford backscattering (RBS) to determine the average elemental composition of the films and low-energy ion scattering (LEIS) to investigate the elemental depth profile of the film composition. The chemical composition of the LSMC thin film surfaces was investigated using X-ray photoelectron spectroscopy (XPS).

The measurement principle of RBS and LEIS involve an ion beam (He^+ and Ne^+) directed onto the solid sample surface from which part of the primary projectiles are backscattered, and the energy distribution of these ions is measured and converted to a mass spectrum by describing the ion-surface atom interaction as a binary collision with conservation of momentum. These are powerful techniques for determining film composition, with RBS able to measure oxygen content and LEIS providing information about the outermost atomic surface terminations.[47,48] In combination with a sputtering ion beam, a depth profile can also be obtained of the chemical composition through the film. Whilst similar, these two techniques provide complementary information due to differences in cross-sections and the electronic excitations and charge transfer processes.[48]

RBS measurements, encompassing the full thickness of the LSMC thin films on LAO and STO substrates (see **Figure 3**), observed that the composition of the thin films is the same regardless of strain, within the uncertainty (due to statistical precision and systematic errors, primarily from calculated He energy loss values). The RBS spectra have flat tops, within the statistical error margins, and RUMP fitting[49] estimated the La/Sr ratio varies by less than 4 % throughout the films (see Figure S8). Target element atomic mass ratios play a key role in determining the composition of thin films deposited by PLD and previous work has demonstrated that lighter elements are often lower in content.[50,51] This accounts for the deviation in the LSMC stoichiometry which has a lower cobalt content compared to bulk LSMC for films under both compressive and tensile strain. However, under the PLD conditions used for these LSMC thin films, there is no corresponding decrease in the manganese concentration which is of both similar atomic mass and has a similar metal-oxygen species stability in the plasma. Variation

of the Co/Mn ratio across the film thickness cannot be estimated from the RBS measurements due to the overlap of the B-site cations signals and a significant background contribution from the substrates. The *stoichiometry* similarity of the LSMC thin films supports the *chemical* similarity observed from the oxygen surface exchange determined by *in situ* XRD measurements.

LEIS was used to obtain a depth-resolved composition profile through the LSMC thin film, encompassing both the air-thin film and thin film-substrate interfaces, by alternating Ne^+ analysis and Ar^+ sputtering beams (see Figure S9). Changes in the signal for each of the elements were analyzed to determine the relative composition of the film as a cross-section through the film thickness. When the signal stabilizes to a constant value, this region is treated as the bulk of the film and taken to be an internal reference, with the stoichiometric ratios defined by RBS. By normalizing the composition of each spectra relative to the internal reference ratio, a depth profile of the surface and near surface regions can be compiled. **Figure 4**a shows a representative depth profile through a LSMC/LSAT thin film where the outermost surface is defined by a zero dose, and the interface between the film and substrate is indicated by the increasing tantalum signal, an element found only in the substrate. Whilst the outermost surface can be represented by a single point, the interface between the thin film and substrate appears as a gradient as the interface is not precisely normal to the ion beam. Ion mixing and roughness below the surface can also broaden the signal.

RBS measurements of the overall film composition suggest a cobalt deficiency within the films that could be related to some Co evaporation during the PLD deposition. LEIS suggests subtle changes in the ratio of manganese to cobalt (see Figure 4d), with a lower ratio at the surface indicative of relatively more cobalt and a higher ratio at the interface indicative of more manganese. B-site enriched sub-surface regions have previously been observed in similar systems and were related to A-site surface segregation.[32,52] For LSMC there is a sub-surface enrichment of cobalt at the B-site in the outermost layers, but an overall B-site deficiency for approximately the top third of the film (see Figure 4c).

The A/B cation ratios established from the LEIS profiles show that all films, regardless of strain, were A-site terminated. Segregation of alkaline-earth dopants to the surface of perovskite oxides is a common occurrence and is usually considered a degradation mechanism, as surface A-cation enrichment can de-activate surface reaction sites and increase resistance.[53] Strontium segregation at perovskite oxide surfaces has been widely reported.[54–56] The strong strontium termination observed (see Figure 4b) is in agreement with recent publications[57,58] and previous work has shown alkaline-earth surface segregation to be associated with elastic and electrostatic interactions of the alkaline-earth with the surrounding lattice, with tensile strain promoting strontium segregation.[34,55] In this work, despite strain significantly altering the unit cell volume of LSMC, no relationship between strontium termination and strain was observed by LEIS or RBS.

In order to quantify the Sr in different chemical environments and understand better the effect of strain on the Sr segregation, XPS analyses were performed. This allowed differentiation of the Sr present in secondary phases such as $Sr(OH)_2$ or $SrCO_3$ from Sr enrichment within the perovskite lattice. In order to perform the XPS analysis the samples were annealed at 300°C to remove carbon contamination. Angle-resolved XPS was performed in order to quantify the different Sr species as a function of depth. The XPS normal to the sample surface showed a slight increase in both oxygen-hydrogen (B.E. ~ 531.5 eV) and carbon (B.E. ~ 285 eV and 288.5 eV) for the films under tensile strain, which can be related to an increase in the strontium segregation in the form of secondary phases (see Figure S10). In perovskites containing

strontium, an insulating phase generally forms on the surface and has been shown to have a majority decomposition product of strontium oxide, SrO, as well as hydroxyl, $Sr(OH)_2$ and carbonate, $SrCO_3$ species.[59,60] Angle-resolved XPS (see **Figure 5**), at emission angles of 60° and 80° between the sample surface normal and the detector position, show clear differences in the strontium environment confirming a higher segregation of Sr in the form of secondary phases under tensile strain These differences are consistent with reported experimental and modelling results for related perovskite systems, where tensile strain has been linked to a surface enrichment of strontium carbonate.[29,30,34,55]. With these results we can conclude that while RBS and LEIS prove the overall Sr content to be similar in the different films, the Sr chemical environment changes as a function of strain proving a higher tendency to form surface Sr-secondary phases with tensile strain.

X-ray absorption near edge spectroscopy (XANES) measurements of the transition metal edge position for the as-deposited LSMC thin films at room temperature (see **Figure 6**a-b) showed that all films were slightly oxygen deficient but that tensile strain favored a more reduced film. Interestingly, we observed that, within the experimental error, the Co oxidation state did not seem to be affected by strain. However, the Mn oxidation state was substantially affected leading to a reduction in oxidation state from 4.1±0.1 to 3.6±0.1. This could be related to the smaller ionic size of Mn(IV) compared with Co(III, HS) in an octahedral environment (0.53 and 0.61 Å, respectively[64]). The shorter Mn-O bond would experience a much greater tensile strain promoting a more facile oxygen release within the Mn octahedra resulting in a lower energy for the formation of oxygen vacancies and larger Mn reduction. Further *in situ* studies were performed with XANES (see Figure S4b and S11) in which thin films were reduced by heating from room temperature to 500°C in hydrogen (O_2 ~ 0.1 ppm) to obtain further chemical information under a more reducing atmosphere. It is noted that the manganese K-edge (6539 eV) is noisy, particularly for LSMC/LAO samples, due to contributions from the lanthanum L_1-edge (6266 eV) which reduce the signal intensity.

For both LSMC/LAO and LSMC/STO, the cobalt and manganese oxidation states reduce as the temperature is increased, as expected for heating under strongly reducing conditions. The differences between the most oxidized and most reduced recorded values are: $\Delta_{Co} = 0.78$ and $\Delta_{Mn} = 1.08$ for LSMC/LAO and $\Delta_{Co} = 0.85$ and $\Delta_{Mn} = 1.15$ for LSMC/STO. For both transition metals, the oxidation states in the LSMC/LAO thin film are relatively less reduced than for LSMC/STO, but for both films there is a greater reduction of the manganese oxidation state supporting our theory of a higher strain induced in the Mn-O bonds. It is also worth noting that Co and Mn seem to be unevenly distributed within the films showing a relatively larger quantity of manganese at the film-substrate interface and a higher segregation of Co in the near-surface. Generally, thin films will have the highest strain at an interface with a single crystal substrate, and relax further from the substrate interface, suggesting that manganese experiences greater strain effects in the strained LSMC films.

3. Conclusion

A fundamental understanding of the effect of strain on the structural and chemical composition of perovskites is crucial to prove the potential of strain-induced oxygen non-stoichiometry systems for practical applications. This work has shown that compressive and tensile strain of the perovskite LSMC result in a linear trend in unit cell volume with strain, demonstrating the impact of strain on the structural properties of LSMC thin films. Extensive characterization of the chemical properties of the LSMC thin films confirmed that these structural changes are also associated with a change in the oxygen content and the surface chemistry of the films. Specifically, we prove that tensile strain favors lower oxygen content that is associated with a higher reduction in the Mn oxidation state. We correlate this to a higher tensile strain-induced

debilitation of the shorter Mn-O bond. Furthermore, tensile strain is proven to induce a higher segregation of Sr secondary phases in the surfaces as suggested by previous studies. Under strong reducing conditions, the role of tensile strain was evident in the greater reduction and stability of the transition metal oxidation states at high temperature, weaker reducing environments could however lead to misleading conclusions if the driving force for further reduction of films is not reached. These results highlight the importance of using *ex situ* and *in situ* complementary techniques to really isolate and understand the effect of strain in the chemistry of thin films.

4. Experimental Section

Bulk material synthesis: LSMC powder was synthesized using a modified Pechini citrate-nitrate synthesis route.[36] Stoichiometric quantities of cobalt (II) nitrate hexahydrate (Sigma Aldrich, ≥ 98 %), strontium nitrate (Sigma Aldrich, ≥ 99 %), lanthanum (III) nitrate hexahydrate (Alfa Aesar, 99.9 %) and manganese (II) acetate tetrahydrate (Alfa Aesar, ≥ 99 %) were mixed with citric acid (10 mass%, ~ 200 cm^3, Sigma Aldrich) and nitric acid (~ 5 cm^3, 68 %, VWR Chemicals). The mixture was dehydrated to form a gel on a hotplate, combusted to remove the solvent (600°C, 12 h, ramp rate: 2°C min^{-1}, cooling rate: 5°C min^{-1}), calcined (800°C, 2 h, ramp rate: 5°C min^{-1}, cooling rate: 10°C min^{-1}) and sintered in air (1150°C, 12 h, ramp rate: 5°C min^{-1}, cooling rate: 10°C min^{-1}). Reduced LSMC was prepared by heating bulk LSMC powder in a tubular furnace (520°C, 8 h, rate: 5°C min^{-1}) whilst flowing 5 % H_2 (BOC, 5 % H_2 / 95 % N_2). After reduction, the powder was stored in an argon glovebox and transferred in a sealed container.

Target synthesis: Bulk LSMC powder was pressed into a pellet, after calcination of the powder, using a uniaxial press (2 t) followed by isostatic pressing (300 MPa) and finally sintering in air (1150°C, 12 h, ramp rate: 5°C min^{-1}, cooling rate: 10°C min^{-1}) before use as the PLD target (ρ = 93 %).

Thin film growth: Thin films of LSMC were deposited onto (001) single crystals of lanthanum aluminate (LAO, $LaAlO_3$), lanthanum aluminate - strontium aluminum tantalate (LSAT, $(LaAlO_3)_{0.3}(Sr_2AlTaO_6)_{0.7}$) and strontium titanate (STO, $SrTiO_3$) from CrysTec GmbH Kristalltechnologie (see Table S1 for lattice parameters). Mismatch between the pseudocubic oxidized LSMC lattice parameter and the substrates was calculated using[37]:

$$f_{LSMC/substrate} = \frac{a_{substrate} - a_{LSMC,ox}}{a_{LSMC,ox}}$$

where *f* is the lattice mismatch and *a* is the lattice parameter. Substrates were single-side epi-polished, single crystals cleaned by sonication in acetone, isopropanol and distilled water prior to deposition. Films were grown by PLD using a KrF excimer laser (λ = 248 nm, Lambda Physik COMPex 201) with a target-to-substrate distance of 128 mm in a modified Neocera combinatorial PLD chamber. Before growth, the substrates were exposed to vacuum (≤ 5 x 10^{-5} Torr) and heated (800°C, ramp: 30°C min^{-1}). The deposition pressure (30 mTorr) was achieved by the introduction of oxygen (BOC). The target was pre-ablated (300 pulses at 4 Hz) to ensure cleanliness of the target surface. LSMC films were deposited at 5 Hz and subsequently cooled (10°C min^{-1}) in an oxygen-rich atmosphere (600 Torr).

Thin film out-of-plane X-ray diffraction: Thin film out-of-plane XRD data was collected using a PANalytical X'Pert Pro MRD diffractometer with parallel beam optics, copper K_α radiation (λ = 1.5418 Å), a 1/16° slit, an X'Celerator detector and a 4-angle goniometer with a crystal monochromator operated at 40 kV and 40 mA. High-resolution XRD was collected using a PANalytical Empyrean diffractometer using a hybrid monochromator (2 x Ge (220)-type channel-cut monochromator), a 4 mm fixed mask, a 1/32° divergence slit and PIXcel3D

Detector. A zero-shift measurement was carried out before all thin film measurements on the PANalytical instruments to ensure no instrumental offsets were present.

In situ X-ray diffraction: *in situ* XRD measurements were performed and data fitted following the method previously described by Moreno et al.[41,42] A Panalytical X'Pert PRO MRD diffractometer was used with a multichannel, fast, linear, solid-state PIXcel detector and a goniometer with a radius of 320 mm with the sample mounted inside an Anton Paar DHS-1100C chamber. The films were heated to 600, 650, 700 and 750°C and cycled between a synthetic air (~ 2.1 x 10^5 ppm, 20 % O_2 / 80 % N_2) and nitrogen (O_2 ~ 10 ppm, 100 % N_2) atmosphere. The cycle times were adjusted depending on the reaction kinetics (from 1 to 4 h), with shorter measurement times at higher temperatures. Gas flushing times were sufficiently fast (≤ 3 s) to neglect this contribution when determining the overall time response of the cell parameters. 2θ scans were collected with an acquisition time interval of 10 s over a range of 2.51° in static mode (255 channels with a resolution of ~ 0.01°) of asymmetrical reflections (ω ≠ θ), namely the cubic $\bar{1}03$ of both the thin film and the substrate. The recorded patterns were fitted with two pseudo-Voigt curves, for the thin film and substrate trace. The thin film peak position was corrected by fixing the position of the substrate (to account for slight variations in the temperature) and the relative c-axis, out-of-plane, parameter was calculated using the equation:[37]

$$c_{parameter} = \frac{\lambda\, l}{2 \sin\theta \cos(\theta - \omega)}$$

where θ is the peak angle, ω is the incident angle, λ is the wavelength of incident X-rays and l is the Miller index of the chosen reflection. The exchange coefficients were extracted by fitting the changes in cell parameter with a two part exponential (reduction, $t_1 < t_2$) or single (oxidation, t_1 only) exponential component in Origin using a Levenberg-Marquart algorithm to find the damped least-squares fit of the (double) exponential decay given by:

$$y = y_0 + A_1 \exp\left(-\frac{x - x_0}{t_1}\right) + A_2 \exp\left(-\frac{x - x_0}{t_2}\right)$$

where y_0 and x_0 are offsets, A is amplitude and t is the decay constant.

Reciprocal space mapping: High-resolution RSM were measured both using a PANalytical X'Pert MRD diffractometer and PANalytical Empyrean, both with a hybrid monochromator (2 x Ge (220)-type channel-cut monochromator). With the X'Pert MRD, the monochromator was mounted with a nickel filter (0.020 mm), a fixed mask (2 mm), a divergence slit (1/2°) and a soller slit (0.4 rad) on the incident beam path. In the diffracted path, a PIXcel detector was used as a 1D linear detector with an anti-scatter slit (7.5 mm). With the Empyrean diffractometer, a fixed mask (4 mm) and a divergence slit (1/32°) were used with a PIXcel3D detector.

X-ray reflectivity: Thickness of the thin films was determined using X-ray reflectivity data collected with a PANalytical Empyrean diffractometer using an incident beam pathway, consisting of a hybrid monochromator (2 x Ge (220)-type channel-cut monochromator), a PreFIX triple-axis analyzer crystal with a proportional detector and an automatic attenuator (Ni 0.125 mm). The thin films were scanned from ~ 0.1 to 2.0° with a step size of ~ 0.005°. PANalytical Reflectivity software, using the Parratt reflectivity formalism,[61] was used to fit a one-dimensional model to the data for the purposes of extracting the thin film thickness. The thickness of the LSMC layer from the thin films used in this study were between ~ 10 to 85 nm.

Rutherford backscattering spectrometry: RBS measurements were performed using a 2 MeV He ion beam and a silicon PIN diode detector mounted at 168° to the incident beam direction. The results were analyzed using the RUMP simulation code.[49] Residual planar channeling in

the substrate was partially compensated in the simulation to obtain a better background fit. The composition was normalized using the condition: La + Sr = 1.

Low energy ion scattering: LEIS data was obtained using an ION-TOF GmbH Qtac instrument under UHV conditions (1.1 x 10^{-8} to 1.8 x10^{-8} mbar) on as-deposited thin films. Incident ions were produced by a heated filament in a He and Ne ion mixed gas atmosphere, accelerated through a potential to achieve energies of 3 keV and 5 keV, for He^+ and Ne^+ respectively. An argon ion beam of 0.5 keV was used for low-energy sputtering with 10 s sputtering intervals and 1 s breaks between sputtering and analysis. Scattered ions were detected at 145° by a double toroidal analyzer. An unfocused electron shower was used to avoid charging of the surface. For the He spectrum of LSMC/STO the dose density used was 2.75 x 10^{14} ions cm^{-2} over an area of 1000 μm^2. For the Ne depth profile of LSMC/STO the dose density of the Ne beam was 2.81 x 10^{15} ions cm^{-2} over an area of 1000 μm^2, and the total dose of the Ar^+ sputtering beam was 4.81 x 10^{17} ions. For the Ne depth profile of LSMC/LAO the dose density of the Ne beam was 1.30 x10^{15} ions cm^{-2} over an area of 1000 μm^2, and the total dose of the Ar^+ sputtering beam was 2.19 x 10^{14} ions. Data is presented after the removal of an exponential background and all analysis was performed using Gaussian fits in IONTOF SurfaceLab 6. The data was collected from multiple areas of measurement on thin films deposited under comparable conditions, with a LSMC layer thickness of ~ 18 nm.

X-ray photoelectron spectroscopy: Spectra were recorded on a Thermo Scientific K-Alpha$^+$ X-ray photoelectron spectrometer operating at 2 x 10^{-9} mbar base pressure. This system incorporates a monochromated, microfocused Al K_α X-ray source ($h\nu$ = 1486.6 eV) and a 180° double focusing hemispherical analyzer with a 2D detector. The X-ray source was operated at 6 mA emission current and 12 kV anode bias providing an X-ray spot size of up to 400 μm^2. Survey spectra were recorded at 200 eV pass energy, 20 eV pass energy for core level. A flood gun was used to minimize the sample charging.

X-ray absorption near edge spectroscopy: XANES measurements were obtained on Beamline B18 at Diamond Light Source, Harwell Science and Innovation Campus, Oxfordshire, operating with a ring energy of 3 GeV and at a current of 300 mA. Manganese and cobalt K-edges were measured in the ranges 6400 to 7200 eV and 7600 to 8300 eV respectively. Calibration of the monochromator was performed using manganese and cobalt metal foils prior to measurement. Thin films were measured in fluorescence with a nine-element germanium detector. The data was analyzed using Athena from the Demeter suite, which implements the FEFF6 and IFEFFIT codes.[62,63] *In situ* measurements were conducted inside a furnace on the Beamline between room temperature and 500°C. The atmosphere in the furnace was evacuated, filled with an inert atmosphere before being placed on the beamline with an atmosphere consisting of hydrogen (Air Products, H_2 4.018 mol%, N_2 95.981 mol%) diluted in nitrogen (Air Products, N_2 BIP, O_2 < 10 ppb, H_2O < 20 ppb, $CO+CO_2$ < 0.5 ppm, CH_4 < 100 ppb, H_2 < 1 ppm) to 3 % H_2 / balance N_2. The furnace had a large interior volume and a porous lining, therefore the experiments were conducted with the furnace over-pressurized to prevent leakage into the furnace.

Supporting Information

Supporting Information is available from the Wiley Online Library or from the author.

Acknowledgements

CvdB, AC, SJS and AA gratefully acknowledge the support of the Engineering and Physical Sciences Research Council (EPSRC) Grants No EP/M014142/1, EP/P026478/1 and EP/L504786/1. CvdB thanks the Royal Society of Chemistry for their Researcher Mobility

Fellowship. We also thank Diamond Light Source for the award of beam time (SP13530 and SP16839). Andrew J. P. White from the Chemical Crystallography Laboratory at Imperial College London is acknowledged for single crystal X-ray diffraction.

Received: ((will be filled in by the editorial staff))
Revised: ((will be filled in by the editorial staff))
Published online: ((will be filled in by the editorial staff))

References

[1] S. B. Adler, *Chem. Rev.* **2004**, *104*, 4791.
[2] J. A. Kilner, M. Burriel, *Annu. Rev. Mater. Res.* **2014**, *44*, 365.
[3] J. Bates, *Solid State Ionics* **2000**, *135*, 33.
[4] M. J. Montenegro, M. Döbeli, T. Lippert, S. Müller, A. Weidenkaff, P. R. Willmott, A. Wokaun, *Appl. Surf. Sci.* **2005**, *247*, 197.
[5] T. Lippert, M. J. Montenegro, M. Döbeli, A. Weidenkaff, S. Müller, P. R. Willmott, A. Wokaun, *Prog. Solid State Chem.* **2007**, *35*, 221.
[6] L. Trotochaud, S. W. Boettcher, *Scr. Mater.* **2014**, *74*, 25.
[7] N. Barsan, D. Koziej, U. Weimar, *Sensors Actuators B Chem.* **2007**, *121*, 18.
[8] R. Waser, M. Aono, *Nat. Mater.* **2007**, *6*, 833.
[9] R. Waser, R. Dittmann, G. Staikov, K. Szot, *Adv. Mater.* **2009**, *21*, 2632.
[10] V. Metlenko, A. H. H. Ramadan, F. Gunkel, H. Du, H. Schraknepper, S. Hoffmann-Eifert, R. Dittmann, R. Waser, R. A. De Souza, *Nanoscale* **2014**, *6*, 12864.
[11] H. L. Tuller, S. R. Bishop, *Annu. Rev. Mater. Res.* **2011**, *41*, 369.
[12] N. H. Perry, T. Ishihara, *Materials (Basel).* **2016**, *9*, 858.
[13] A. Fluri, D. Pergolesi, V. Roddatis, A. Wokaun, T. Lippert, *Nat. Commun.* **2016**, *7*, 10692.
[14] A. Fluri, A. Marcolongo, V. Roddatis, A. Wokaun, D. Pergolesi, N. Marzari, T. Lippert, *Adv. Sci.* **2017**, *4*, 1700467.
[15] J.-P. Locquet, J. Perret, J. Fompeyrine, E. Mächler, J. W. Seo, G. Van Tendeloo, *Nature* **1998**, *394*, 453.
[16] G. F. Harrington, S. J. Skinner, J. A. Kilner, *J. Am. Ceram. Soc.* **2018**, *101*, 1310.
[17] B. Yildiz, *MRS Bull.* **2014**, *39*, 147.
[18] A. Kushima, B. Yildiz, *J. Mater. Chem.* **2010**, *20*, 4809.
[19] G. F. Harrington, L. Sun, B. Yildiz, K. Sasaki, N. H. Perry, H. L. Tuller, *Acta Mater.* **2019**, *166*, 447.
[20] B. Hammer, J. K. Nørskov, *Surf. Sci.* **1995**, *343*, 211.
[21] J. K. Nørskov, J. Rossmeisl, A. Logadottir, L. Lindqvist, J. R. Kitchin, T. Bligaard, H. Jónsson, *J. Phys. Chem. B* **2004**, *108*, 17886.
[22] J. Suntivich, H. A. Gasteiger, N. Yabuuchi, H. Nakanishi, J. B. Goodenough, Y. Shao-Horn, *Nat. Chem.* **2011**, *3*, 546.
[23] J. Suntivich, K. J. May, H. A. Gasteiger, J. B. Goodenough, Y. Shao-Horn, *Science* **2011**, *334*, 1383.
[24] J. Jung, H. Y. Jeong, J. Lee, M. G. Kim, J. Cho, *Angew. Chem. Int. Ed. Engl.* **2014**, *53*, 4582.
[25] J.-I. Jung, S. Park, M.-G. Kim, J. Cho, *Adv. Energy Mater.* **2015**, *5*, 1501560.
[26] A. Herklotz, D. Lee, E.-J. Guo, T. L. Meyer, J. R. Petrie, H. N. Lee, *J. Phys. Condens. Matter* **2017**, *29*, 493001.
[27] D. O. Klenov, W. Donner, B. Foran, S. Stemmer, *Appl. Phys. Lett.* **2003**, *82*, 3427.
[28] M. Kubicek, Z. Cai, W. Ma, B. Yildiz, H. Hutter, J. Fleig, *ACS Nano* **2013**, *7*, 3276.
[29] Z. Cai, Y. Kuru, J. W. Han, Y. Chen, B. Yildiz, *J. Am. Chem. Soc.* **2011**, *133*, 17696.
[30] Y. Yu, K. F. Ludwig, J. C. Woicik, S. Gopalan, U. B. Pal, T. C. Kaspar, S. N. Basu, *ACS*

Appl. Mater. Interfaces **2016**, *8*, 26704.
[31] H. Dulli, P. A. Dowben, S.-H. Liou, E. W. Plummer, *Phys. Rev. B* **2000**, *62*, R14629.
[32] Y. Chen, H. Téllez, M. Burriel, F. Yang, N. Tsvetkov, Z. Cai, D. W. McComb, J. A. Kilner, B. Yildiz, *Chem. Mater.* **2015**, 150630082136008.
[33] H. Jalili, J. W. Han, Y. Kuru, Z. Cai, B. Yildiz, *J. Phys. Chem. Lett.* **2011**, *2*, 801.
[34] W. Lee, B. Yildiz, *ECS Trans.* **2013**, *57*, 2115.
[35] W. Lee, J. W. Han, Y. Chen, Z. Cai, B. Yildiz, *J. Am. Chem. Soc.* **2013**, *135*, 7909.
[36] A. Aguadero, H. Falcon, J. M. Campos-Martin, S. M. Al-Zahrani, J. L. G. Fierro, J. A. Alonso, *Angew. Chemie* **2011**, *123*, 6687.
[37] M. Birkholz, *Thin Film Analysis by X-Ray Scattering*; Wiley-VCH: Darmstadt, Germany, 2006.
[38] J. L. M. Rupp, *Solid State Ionics* **2012**, *207*, 1.
[39] T. Mayeshiba, D. Morgan, *Phys. Chem. Chem. Phys.* **2015**, *17*, 2715.
[40] J. R. Petrie, C. Mitra, H. Jeen, W. S. Choi, T. L. Meyer, F. A. Reboredo, J. W. Freeland, G. Eres, H. N. Lee, *Adv. Funct. Mater.* **2016**, *26*, 1564.
[41] R. Moreno, P. García, J. Zapata, J. Roqueta, J. Chaigneau, J. Santiso, *Chem. Mater.* **2013**, *25*, 3640.
[42] R. Moreno, J. Zapata, J. Roqueta, N. Bagues, J. Santiso, *J. Electrochem. Soc.* **2014**, *161*, F3046.
[43] J. Santiso, R. Moreno, In *Electro-Chemo-Mechanics of Solids*; Bishop, S. R.; Perry, N. H.; Marrocchelli, D.; Sheldon, B. W., Eds.; Springer International Publishing, 2017; pp. 35–60.
[44] R. De Souza, J. A. Kilner, *Solid State Ionics* **1998**, *106*, 175.
[45] R. . De Souza, J. . Kilner, *Solid State Ionics* **1999**, *126*, 153.
[46] S. R. Bishop, D. Marrocchelli, C. Chatzichristodoulou, N. H. Perry, M. B. Mogensen, H. L. Tuller, E. D. Wachsman, *Annu. Rev. Mater. Res.* **2014**, *44*, 205.
[47] H. H. Brongersma, M. Draxler, M. De Ridder, P. Bauer, *Surf. Sci. Rep.* **2007**, *62*, 63.
[48] *Surface Analysis – The Principal Techniques*; Vickerman, J. C.; Gilmore, I. S., Eds.; Second.; John Wiley & Sons, Ltd: Singapore, 2009.
[49] L. R. Doolittle, *Nucl. Instruments Methods Phys. Res. Sect. B Beam Interact. with Mater. Atoms* **1986**, *15*, 227.
[50] A. Ojeda-G-P, M. Döbeli, T. Lippert, *Adv. Mater. Interfaces* **2018**, *5*, 1.
[51] J. Chen, M. Döbeli, D. Stender, K. Conder, A. Wokaun, C. W. Schneider, T. Lippert, *Appl. Phys. Lett.* **2014**, *105*, 114104.
[52] J. Druce, H. Téllez, M. Burriel, M. D. Sharp, L. J. Fawcett, S. N. Cook, D. S. McPhail, T. Ishihara, H. H. Brongersma, J. A. Kilner, *Energy Environ. Sci.* **2014**, *7*, 3593.
[53] H. Ding, A. V. Virkar, M. Liu, F. Liu, *Phys. Chem. Chem. Phys.* **2013**, *15*, 489.
[54] N. Caillol, M. Pijolat, E. Siebert, *Appl. Surf. Sci.* **2007**, *253*, 4641.
[55] T. T. Fister, D. D. Fong, J. A. Eastman, P. M. Baldo, M. J. Highland, P. H. Fuoss, K. R. Balasubramaniam, J. C. Meador, P. A. Salvador, *Appl. Phys. Lett.* **2008**, *93*, 151904.
[56] G. M. Rupp, H. Téllez, J. Druce, A. Limbeck, T. Ishihara, J. A. Kilner, J. Fleig, *J. Mater. Chem. A* **2015**, *3*, 22759.
[57] M. Burriel, S. Wilkins, J. P. Hill, M. A. Muñoz-Márquez, H. H. Brongersma, J. A. Kilner, M. P. Ryan, S. J. Skinner, *Energy Environ. Sci.* **2014**, *7*, 311.
[58] J. Druce, T. Ishihara, J. A. Kilner, *Solid State Ionics* **2014**, *262*, 893.
[59] W. Jung, H. L. Tuller, *Energy Environ. Sci.* **2012**, *5*, 5370.
[60] D. Newby, J. Kuyyalil, J. Laverock, K. F. Ludwig, Y. Yu, J. Davis, S. Gopalan, U. B. Pal, S. Basu, K. E. Smith, *Thin Solid Films* **2015**, *589*, 655.
[61] L. Parratt, *Phys. Rev.* **1954**, *95*, 359.
[62] B. Ravel, M. Newville, *J. Synchrotron Radiat.* **2005**, *12*, 537.
[63] M. Newville, *J. Synchrotron Radiat.* **2001**, *8*, 96.

[64] R. D. Shannon, Acta Cryst. 1976, A32, 751

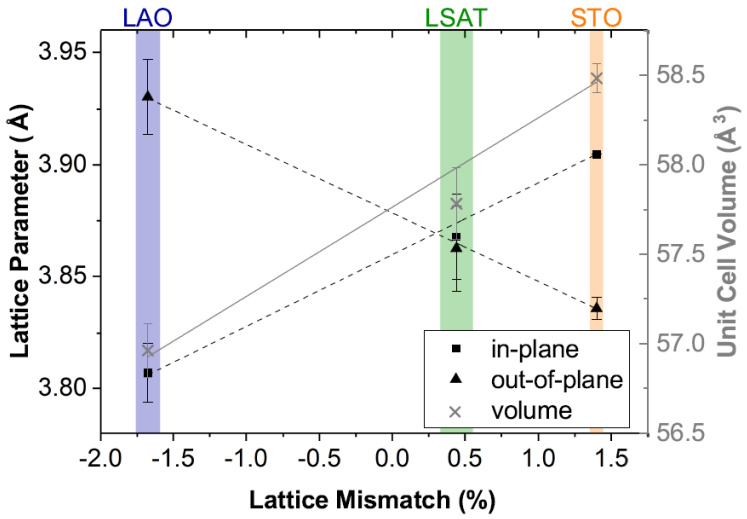

Figure 1. In-plane (squares) and out-of-plane (triangles) cell parameters and average unit cell volume (crosses) of LSMC thin films. Uncertainties represent the standard deviation in the measurements. Lines are to guide the eye and show the inverse relationship between the unit cell parameters (black) and the increase in volume (grey) with increasing tensile strain.

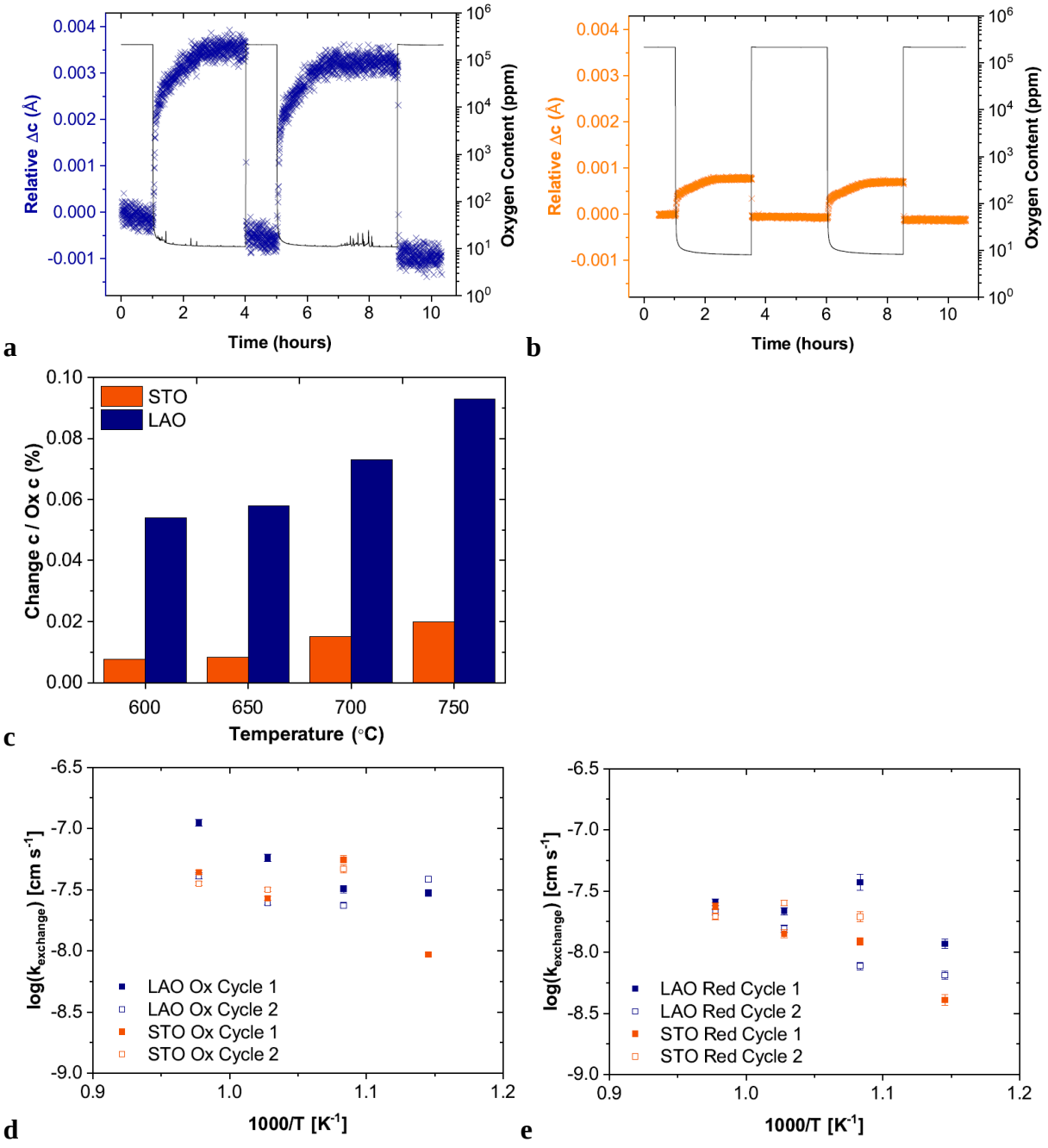

Figure 2. Example of relative out-of-plane cell, c, parameters for LSMC thin film layer at 750 °C for (a) LSMC/LAO and (b) LSMC/STO, the data has been presented on comparable axes showing the cell parameter changes and the related oxygen content (black). (c) Change in LSMC out-of-plane cell parameter between high and low oxygen environments, over the measured temperature range of 600 to 750°C. Arrhenius plots showing the temperature dependence of oxygen surface exchange for LSMC/LAO (blue) and LSMC/STO (orange) during (d) oxidation and (e) reduction.

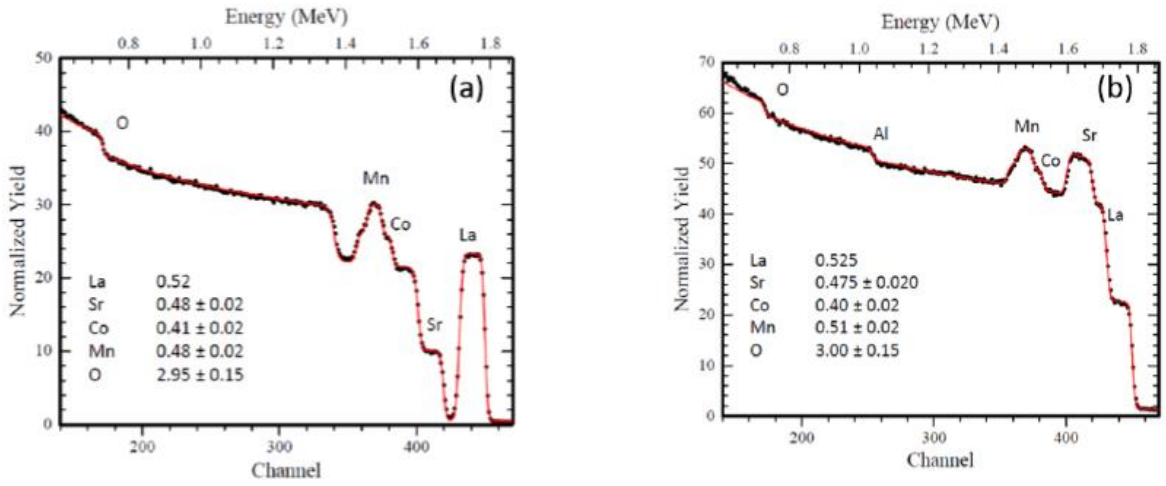

Figure 3. RBS of (a) LSMC/STO and (b) LSMC/LAO with the results of the RUMP fitting (red) inset to tabulate the stoichiometry of the LSMC thin films. The signal is an overlay of the depth profile of all elements of the thin films and substrates, and as scattering cross-sections are proportional to the atomic number squared, oxygen has a greater uncertainty than heavier elements.

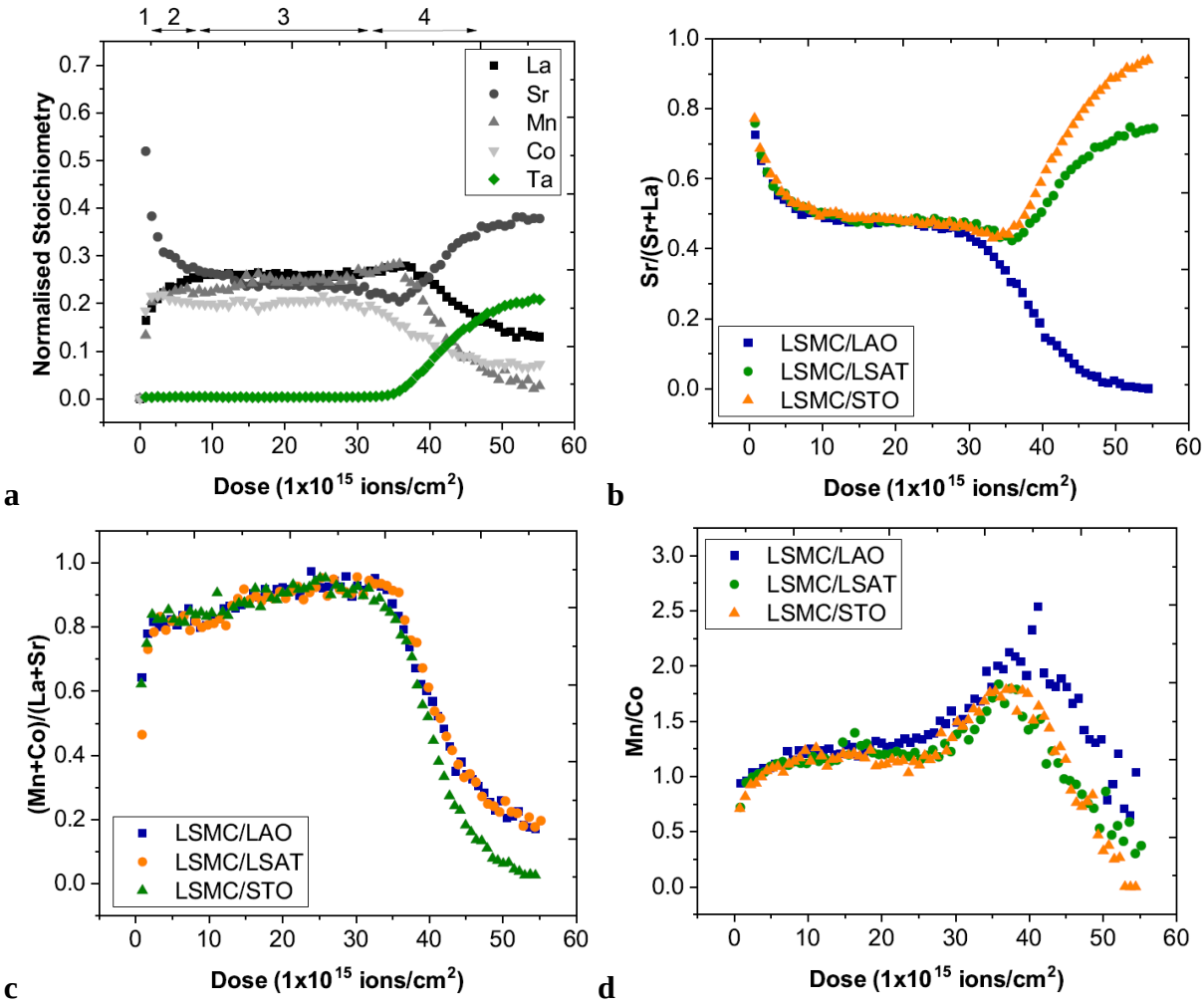

Figure 4. (a) Depth profile of a LSMC/LSAT thin film from LEIS data collected using a 5 keV $^{20}Ne^{+}$ analysis ion beam and alternating with 10 s sputtering using a 0.5 keV $^{40}Ar^{+}$ ion beam, normalized to the average LSMC stoichiometry from RBS. Four regions in the depth profile are indicated: (1) outermost surface, (2) sub-surface, (3) "bulk" thin film and (4) film-substrate interface. The tantalum signal is included to indicate the interface with the substrate. (b) Fraction of strontium cations to the total A-site component (strontium and lanthanum). (c) Ratio of total A-site and B-site cations. (d) Ratio of manganese and cobalt at the B-site.

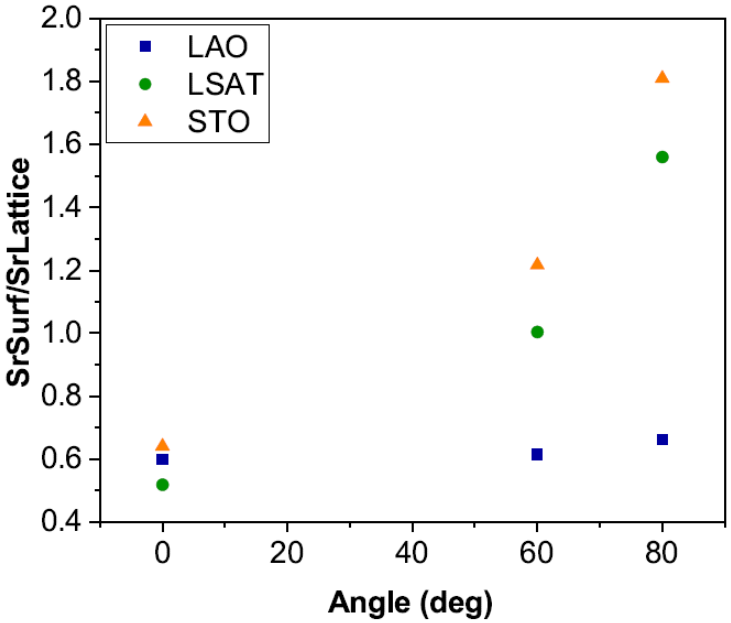

Figure 5. Ratio of $Sr3d_{5/2}$ signals for Sr-O lattice $SrCO_3$ surface peak areas at both angles normal (0°) and glancing to the surface (60° and 80°). The higher ratio at higher angles for LSMC/LSAT and LSMC/STO suggests greater strontium carbonate at the surface of films under tensile strain. The accuracy of XPS atomic concentrations is within **2%**.

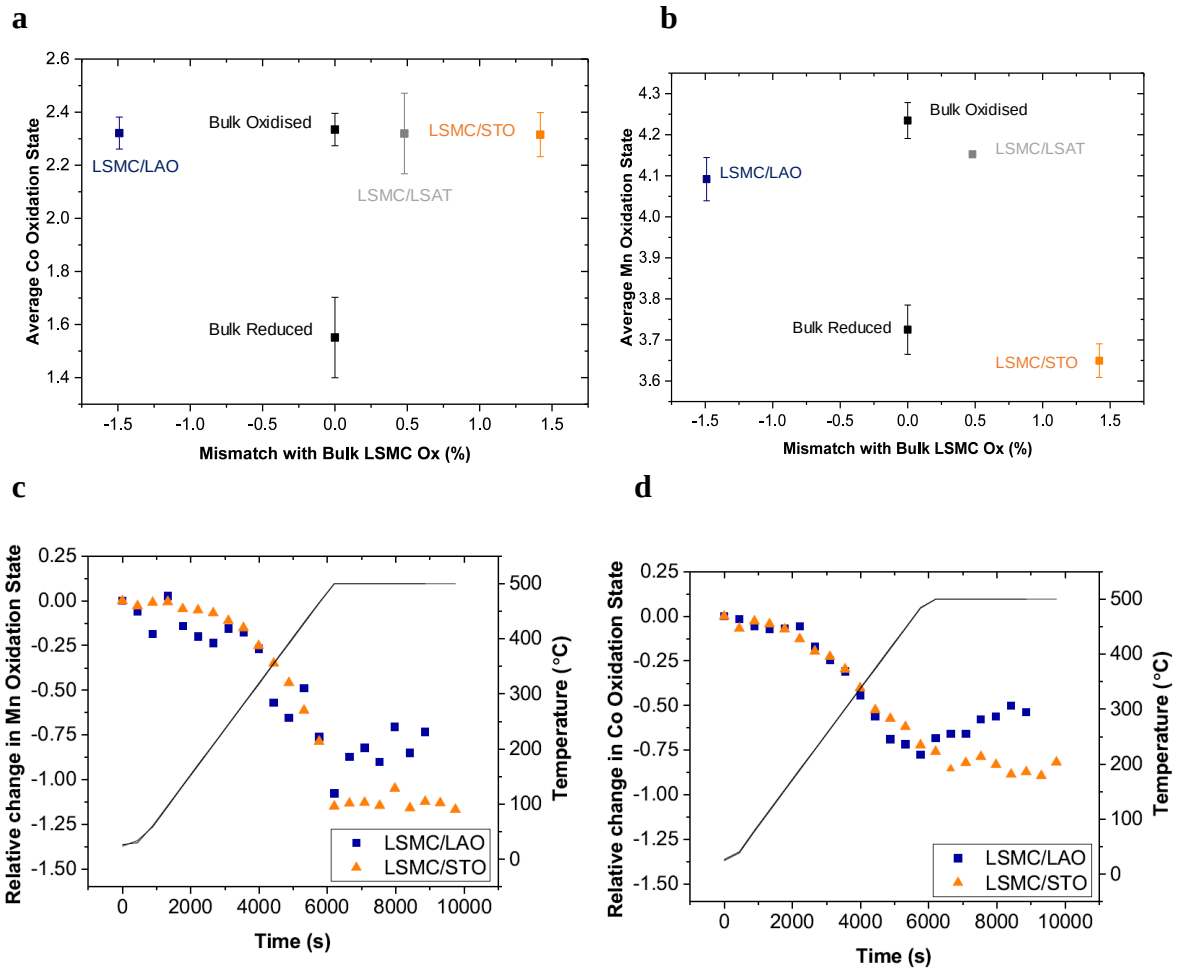

Figure 6. Average oxidation states for (a) cobalt and (b) manganese of as-deposited LSMC thin films. The Mn K-edge show glitches in both the pre-edge and normalization region, due to its lower intensity as a result of interference from the La L_1-edge. Relative changes in the oxidation states of (c) cobalt and (d) manganese for LSMC/LAO (blue squares) and LSMC/STO (orange triangles) as determined during *in situ* XANES when heating the samples from room temperature to 500°C under a strongly reducing atmosphere of 3 % H_2 / 97% N_2.

Table of Contents Entry

The structure, composition and chemistry of strained epitaxial thin films of the perovskite $La_{0.5}Sr_{0.5}Mn_{0.5}Co_{0.5}O_{3-\delta}$ (LSMC) are characterized as deposited and *in situ* using complementary methods including X-ray diffraction, X-ray absorption near edge spectroscopy and ion scattering techniques. The induced strain primarily resulted in structural changes, B-site metal oxidation state is energetically driven by the constrained B-O bond length that induced preferential reduction of Mn cations and increase the segregation of Sr in the surface leasing to formation of passivating secondary phases.

Thin films

Celeste A. M. van den Bosch, Andrea Cavallaro, Roberto Moreno, Giannantonio Cibin, Gwilherm Kerherve, José M. Caicedo, Thomas K. Lippert, Max Doebeli, José Santiso, Stephen J. Skinner and Ainara Aguadero**

Revealing strain effects on the chemical composition of perovskite oxide thin films surface, bulk and interfaces

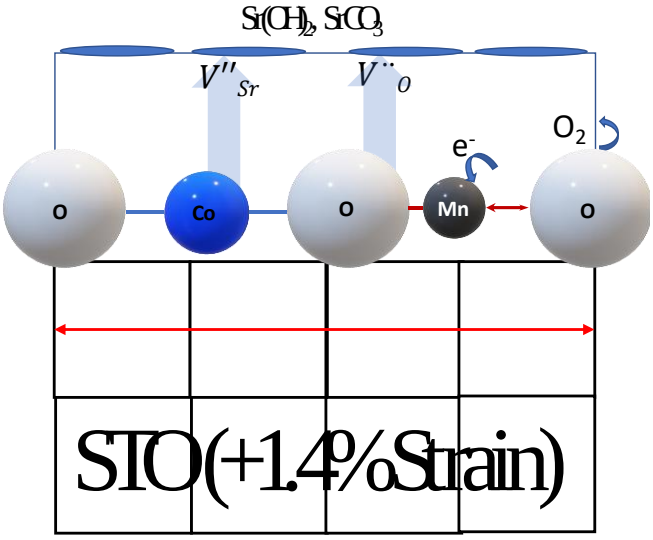

Supporting Information

In Situ Investigation of Strain Effects on Mechanical and Chemical Properties of Epitaxial $La_{0.5}Sr_{0.5}Mn_{0.5}Co_{0.5}O_{3-\delta}$ Thin Films

Celeste A. M. van den Bosch, Andrea Cavallaro, Roberto Moreno, Giannantonio Cibin, Gwilherm Kerherve, José M. Caicedo, Thomas K. Lippert, Max Doebeli, José Santiso, Stephen J. Skinner and Ainara Aguadero**

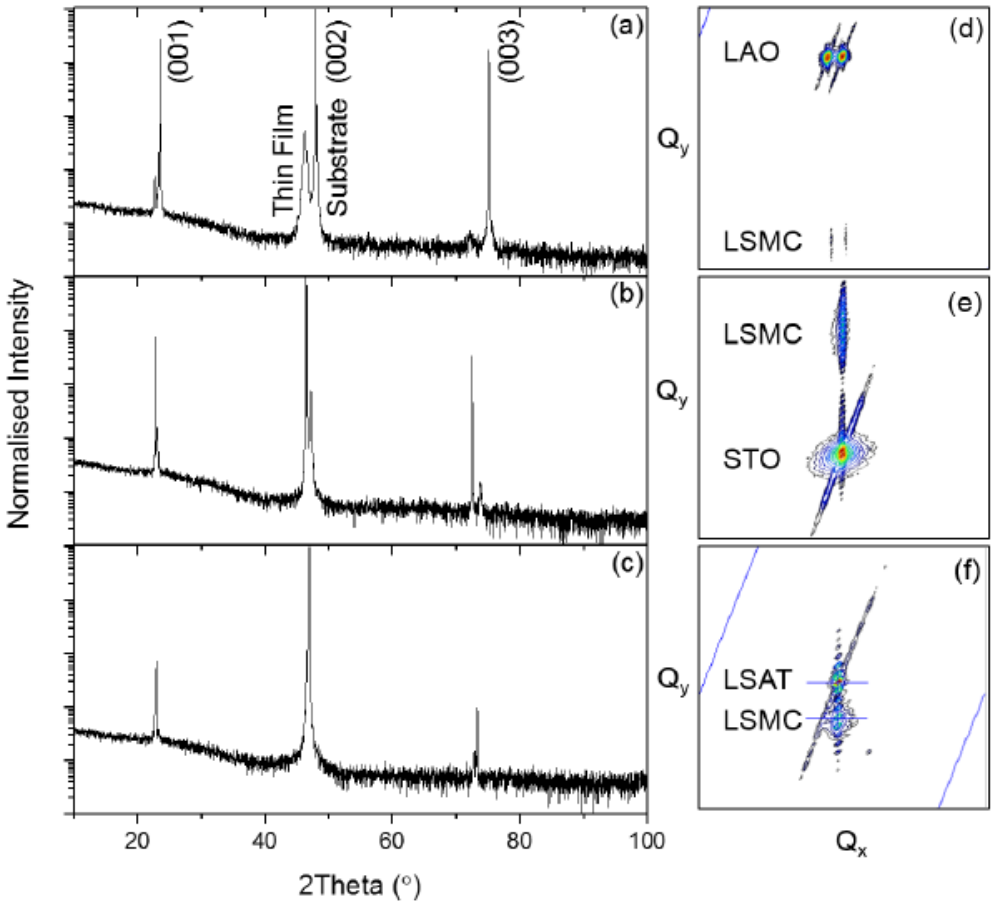

Figure S1. XRD (a-c) and RSM of the ($\bar{1}03$) Bragg reflection (d-f) of epitaxial LSMC thin films on LAO (a, d), STO (b, e) and LSAT (c, f). Diffraction peaks relating solely to the (00*l*) reflections were observed, confirming single phase, epitaxial growth of LSMC with (00*l*) planes of the films parallel to the substrate surfaces. Epitaxial growth and thin film quality were confirmed with high-resolution XRD. RSM of the ($\bar{1}03$)Bragg reflection, measured at room temperature, shows alignment of the substrates and LSMC thin films in Q_x, confirming the LSMC films are fully strained in-plane. For LSMC/LAO there are two peaks for both the substrate and thin film due to known twinning of the LAO substrate. Broadening of the XRD peaks for the LSMC thin film are related to the thickness of the films and relaxation of strain away from the interface.

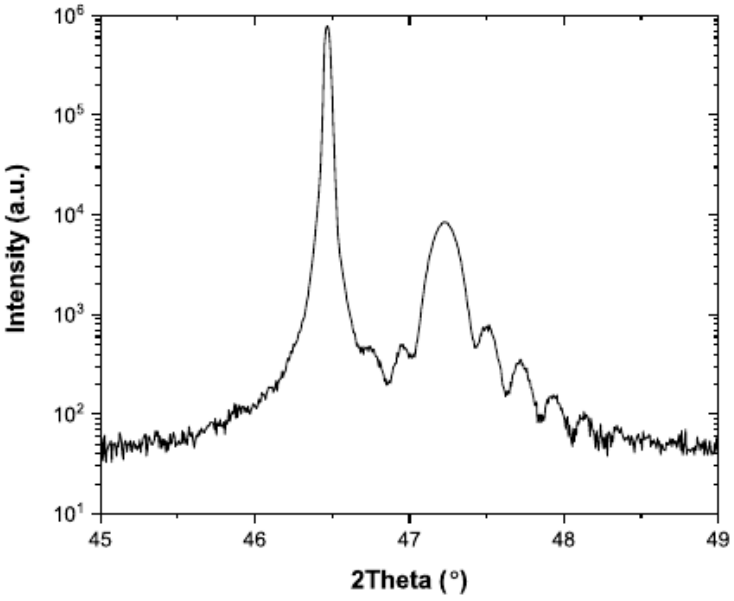

Figure S2. High-resolution XRD of a LSMC/STO sample showing Kiessig fringes, confirming growth of a highly oriented film.

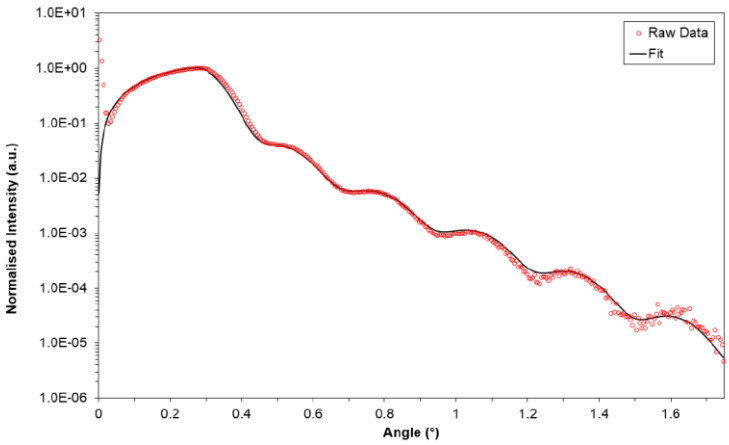

Figure S3. Example of fitting (black line) of an XRR scan (red circles) of an LSMC/STO thin film of ~ 15.34 nm.

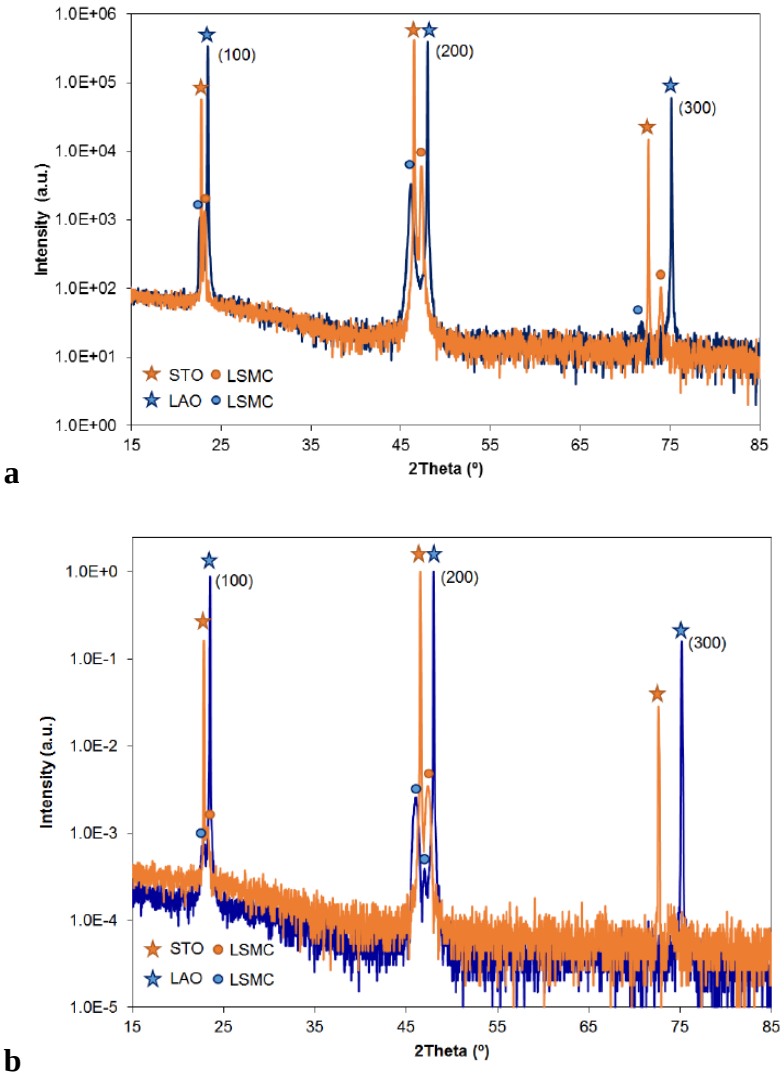

Figure S4. Out-of-plane XRD pattern of LSMC thin films grown on LAO (blue) and STO (orange) showing *h*00 peaks of the substrate (stars) and LSMC thin film peaks (circles) from the samples used for the (a) *in situ* XRD and (b) *in situ* XANES studies presented in the main manuscript. There are three peaks visible for each sample, relating to the *h*00 reflections and the lack of peaks at other 2θ values indicates the epitaxial growth of the films.

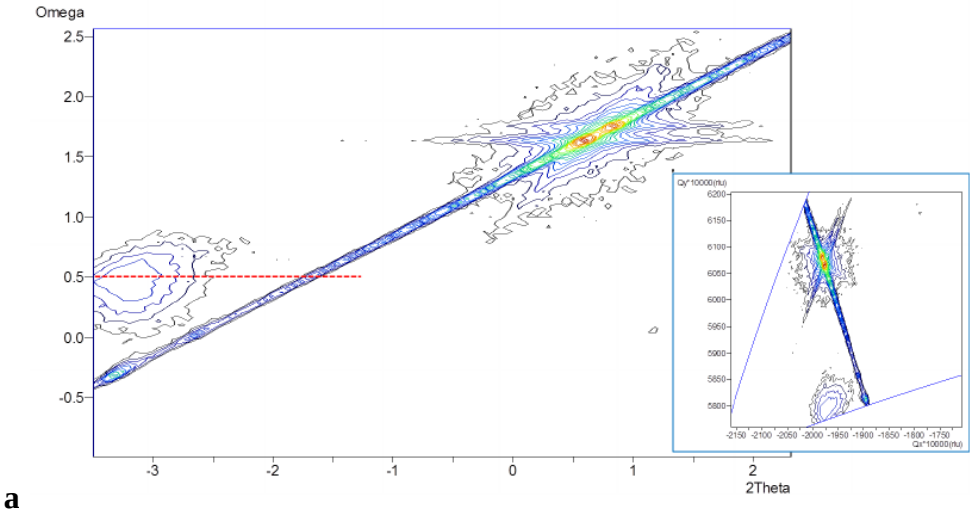

a

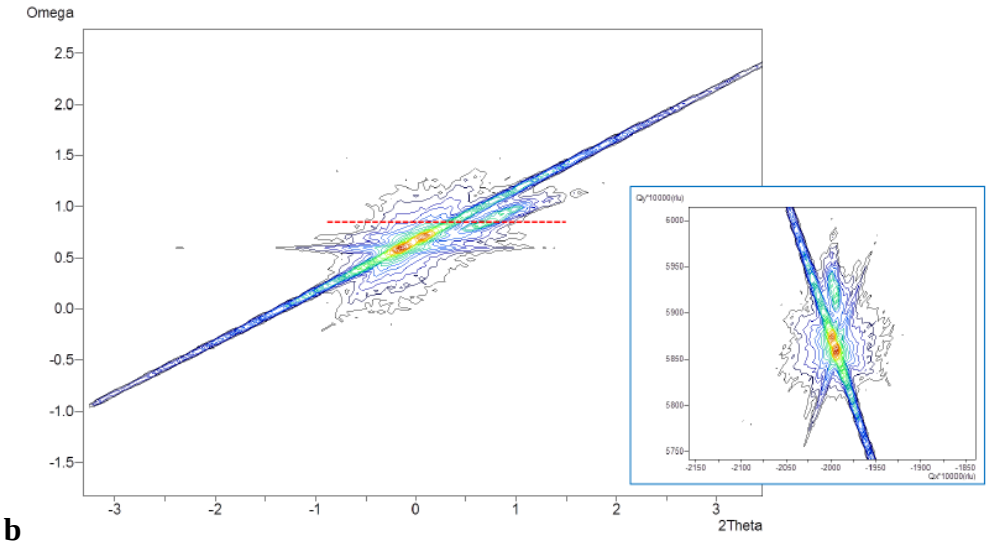

b

Figure S5. RSM of the ($\bar{1}03$) reflection under reducing conditions, 100% N_2, at 750°C for (a) LSMC/LAO and (b) LSMC/STO. The red dotted line indicates the approximate region measured during the *in situ* 2θ scans at a fixed omega value, which passes through the maximum of the LSMC thin film peak. The insets include the RSM data in reciprocal space (Q_x, Q_y) where the alignment of the thin films to the substrates, used to calculate strain in the films, is more easily observed. In the LSMC/LAO film, there is evidence of relaxation due to the spread of the data for the thin film ($\bar{1}03$) reflection.

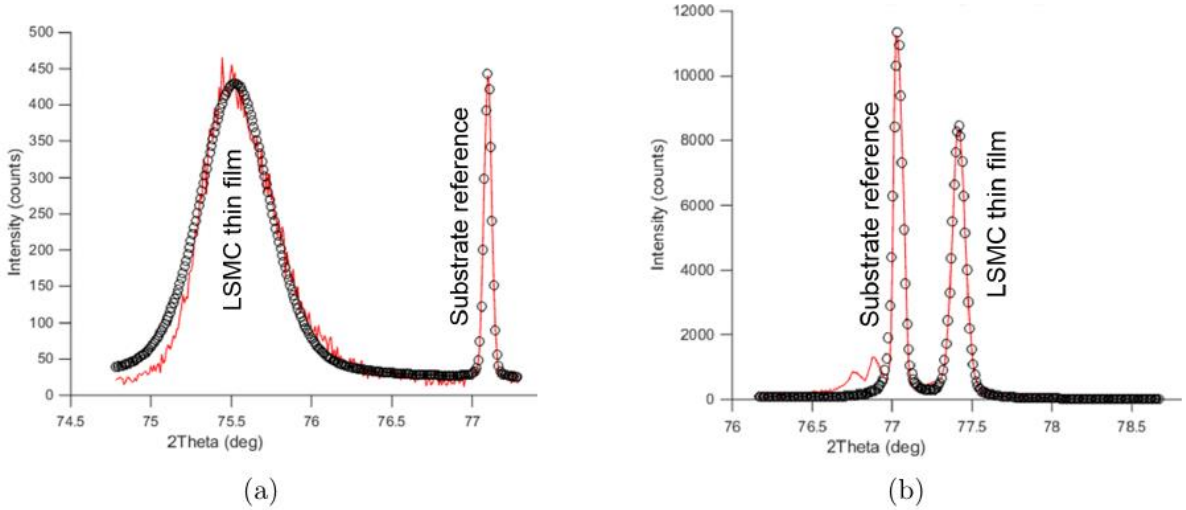

Figure S6. Single, static 2θ line scan plotted for raw (red) and pseudo-Voigt fitted (black) data of a single *in situ* XRD scan of 2θ = 2.5° for (a) LSMC/LAO and (b) LSMC/STO.

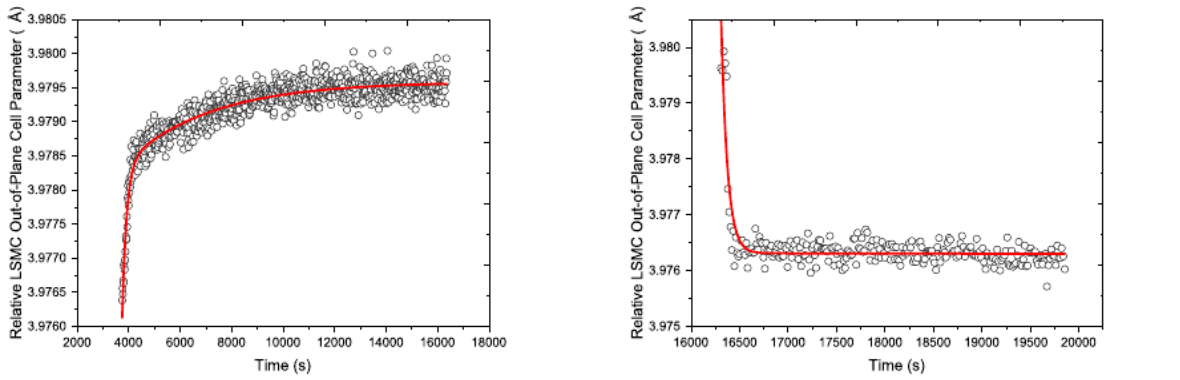

(a) Example fitting of reduction using a two-component exponential.

(b) Example fitting of oxidation using a single exponential factor.

Figure S7. Example exponential fitting (red) of the change in the LSMC/LAO cell parameter at 700°C to determine the time response when cycling between synthetic air and nitrogen.

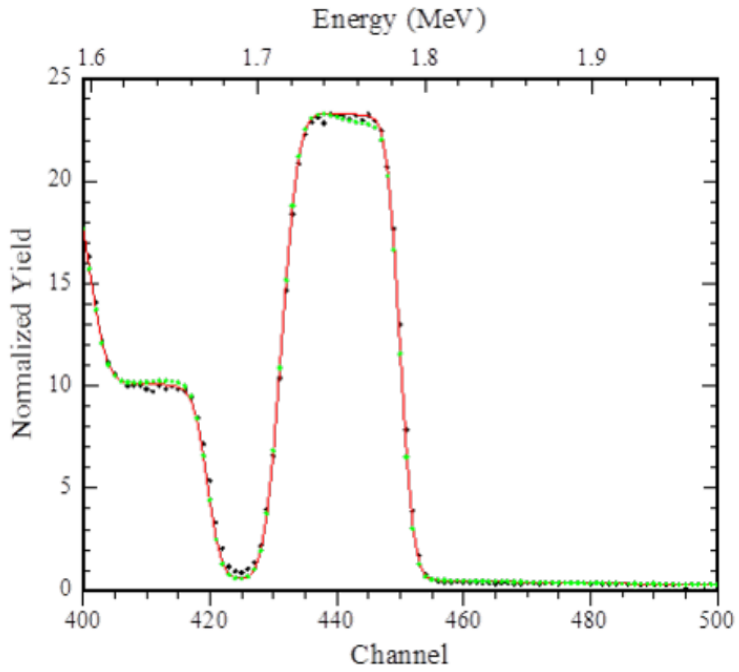

Figure S8. Example of RBS fitting of the La signal, which is almost background free for a LSMC/STO thin film of ~ 85 nm thickness. The red line is the simulation for La/Sr ratio of 0.52/0.48. The green dots correspond to a situation where the ratio is 0.51/0.49 at the surface (to the right) and 0.52/0.49 at the interface (to the left). From this, it is estimated that the La/Sr ratio varies by less than 4 % throughout the film. The Co/Mn ratio was not investigated in detail as these two signals overlap and there is a significant contribution from the substrates.

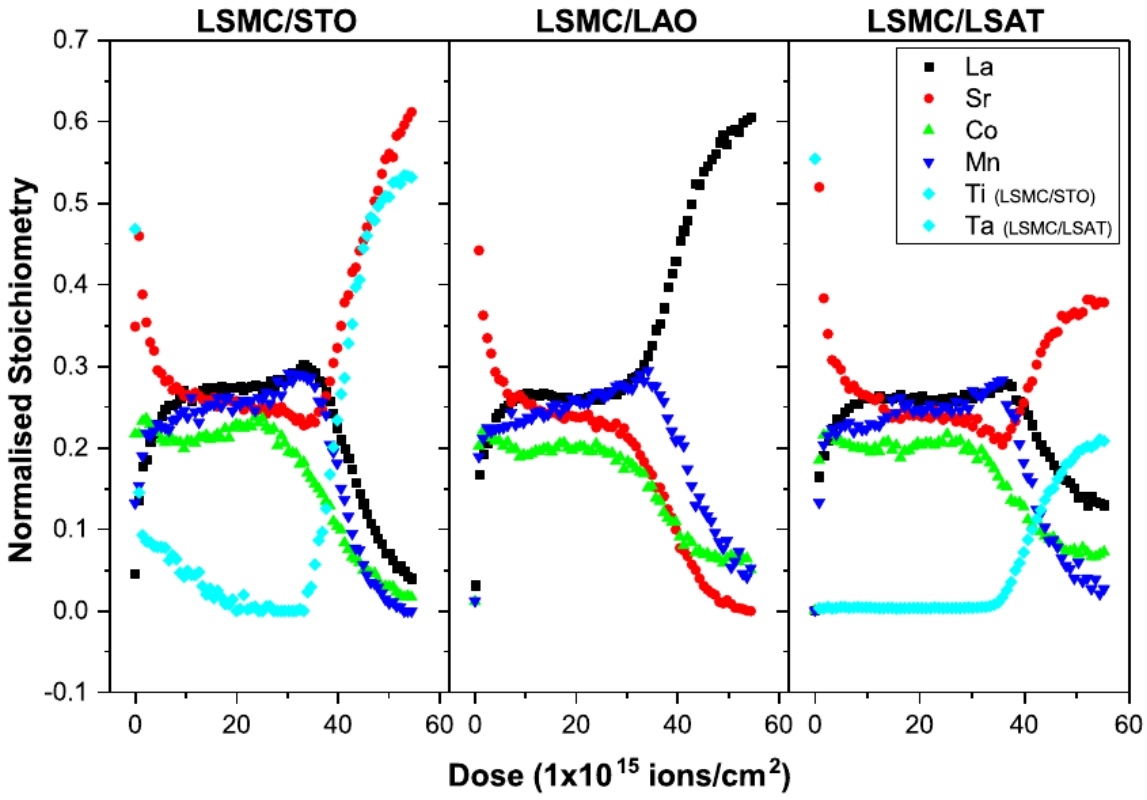

Figure S9. LEIS depth profiles collected using a 5 keV $^{20}Ne^{+}$ analysis ion beam and alternating with 10 s sputtering using a 0.5 keV $^{40}Ar^{+}$ ion beam. Data normalized to the bulk LSMC composition determined by RBS.

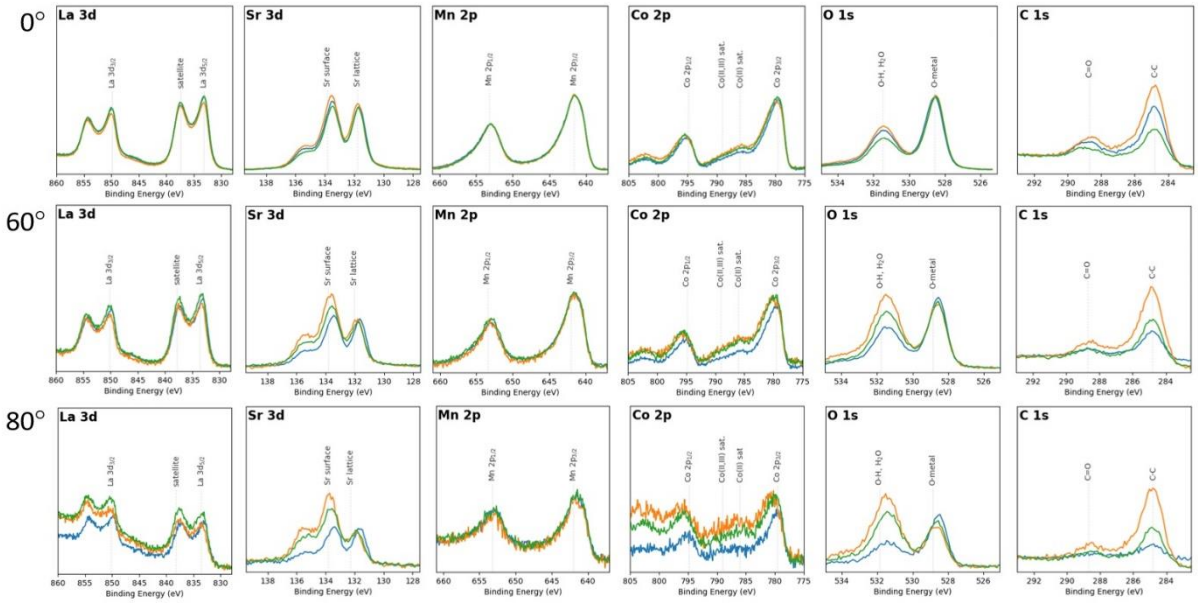

Figure S10. Angle-resolved XPS for LSMC/LAO (blue), LSMC/LSAT (green) and LSMC/STO (blue) after Shirley correction and normalized to Mn $2p_{3/2}$.

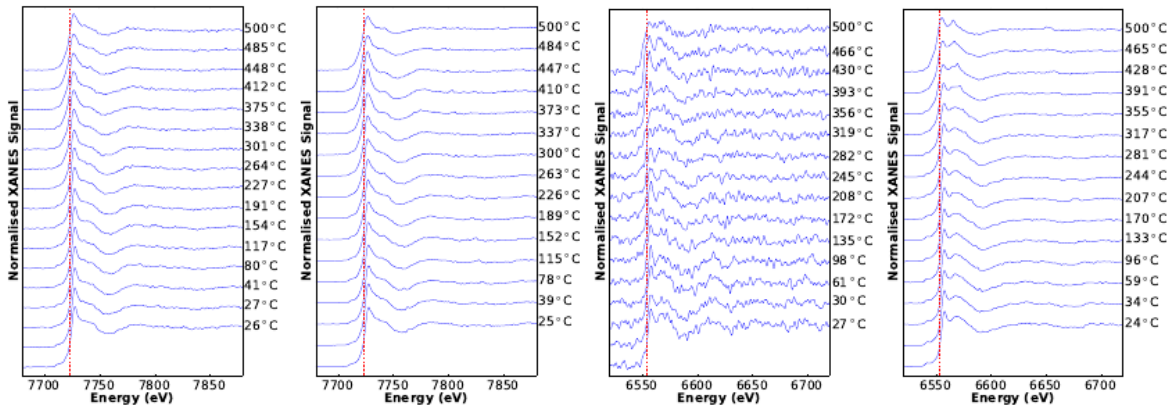

(a) Co K-edge LSMC/LAO (b) Co K-edge LSMC/STO (c) Mn K-edge LSMC/LAO (d) Mn K-edge LSMC/STO

Figure S11. Normalized scans of Co and Mn K-edges while heating the LSMC thin films from room temperature to 500°C under reducing conditions, 3 % H_2 / 97 % N_2. The red dashed lines indicate the edge position at the first temperature. Due to the post-edge region of the lanthanum signal there is a reduction in the quality of the manganese signal (K-edge of metallic Mn at 6539 eV}), particularly for the LSMC/LAO film which has the contribution of La L_1-edge (6266 eV) from both the substrate and thin film. During heating under reducing conditions, the films are reduced, which results in a shift of edge position to lower energies.

Table S1. Lattice parameters of the single crystal substrates measured by single crystal XRD at the Chemical Crystallography Laboratory at Imperial College London.

Substrate	**LAO**	**LSAT**	**STO**
a [Å]	3.787(3)	7.718(3)	3.896(2)
b [Å]	3.76(2)	7.714(6)	3.8982(18)
c [Å]	3.780(5)	7.722(2)	3.914(7)
α [°]	90.00(7)	90.07(4)	89.94(8)
β [°]	90.06(9)	90.01(3)	89.99(8)
γ [°]	90.05(5)	89.93(4)	89.97(4)